

Dynamic similarity of vortex shedding in a superfluid flowing past a penetrable obstacle

Junhwan Kwon^{1,2} and Y. Shin^{1,2,3,*}

¹*Department of Physics and Astronomy, Seoul National University, Seoul 08826, Korea*

²*NextQuantum, Seoul National University, Seoul 08826, Korea*

³*Institute of Applied Physics, Seoul National University, Seoul 08826, Korea*

We numerically investigate wake dynamics in a superfluid flowing past a penetrable obstacle. The penetrable obstacle does not fully deplete the density, and we define an effective diameter D_{eff} from the Mach-1 contour of the time-averaged irrotational flow around the obstacle, which delineates the local supersonic region where quantized vortices nucleate. Using this flow-defined length, we construct a superfluid Reynolds number $\text{Re}_s \equiv (v_0 - v_c)D_{\text{eff}}/(\hbar/m)$ with v_0 being the flow speed, v_c as the critical velocity and m as the particle mass, and show that Re_s organizes the wake dynamics across obstacle sizes and strengths: the transition from dipole-row emission to alternating vortex cluster shedding occurs for $\text{Re}_s \approx 2$ and the Strouhal number and drag coefficient collapse onto universal curves versus Re_s . These results extend the notion of dynamic similarity in superfluid flows to penetrable obstacles and demonstrate that the dynamically relevant length scale is determined by the supersonic region rather than by the geometric obstacle size.

I. INTRODUCTION

Dynamic similarity refers to the principle that flows, with different absolute scales of length, time, and mass in fluid properties, can exhibit identical behavior when expressed in terms of appropriate dimensionless parameters [1]. A paradigmatic example is a flow past bluff bodies, where wake transitions and forces are organized according to the Reynolds number $\text{Re} = UD/\nu$ [2], where U is the flow velocity, D is the characteristic length of the body and ν is the kinematic viscosity. Above $\text{Re} \approx 50$ [3], a periodic alternating vortex pattern, known as the von Kármán vortex street, starts to form, and for larger values of Re , the wake gradually loses strict periodicity, entering turbulent vortex shedding around $\text{Re} = 250$ [4]. Nevertheless, the lift force, normal to the direction of the background flow, still has a dominant frequency. The shedding frequency f_s is nondimensionalized through the Strouhal number $\text{St} = f_s D/U$, showing universal $\text{St}-\text{Re}$ trends over broad ranges of Re , where $\text{St} \approx 0.2$, nearly up to nearly $\text{Re} \sim 10^5$ [2, 5]. Moreover, when the drag force F_D is normalized to the coefficient $C_D = F_D/(\frac{1}{2}\rho U^2 A)$, where ρ is the mass density of the fluid and A is the reference area of the object, it exhibits well-known dependence on the Reynolds number [6, 7], typically taking values of $C_D \sim 1$ over a broad range of $\text{Re} \sim 10^3 - 10^5$ [4].

The advent of quantum fluids has enabled tests of such universality of dynamic similarity in new regimes. Liquid helium systems have long served as a platform for research on inviscid flows [8–10], and ultracold atomic gases now provide an especially clean and highly controllable system, where versatile flow geometries can be engineered by optical methods with high precision. In these systems, one can investigate the properties of dissipationless fluids

and probe exotic phenomena unique to superfluids, such as the nucleation and dynamics of quantized vortices [11–16]. An increasing number of studies have highlighted ensuing parallels between classical and quantum flows. The von Kármán vortex streets behind obstacles [17–21], the scaling law in quantum turbulence [22–24] and universal scaling along with the superfluid Reynolds number in shedding dynamics [25–27] represent cases in which well-known concepts in classical fluid dynamics can be extended to quantum cases. Recently, it was theoretically shown that dissipation in classical fluids can be understood through the Josephson–Anderson relation for superfluids [28] presenting a case where knowledge pertaining to superfluids offers valuable insight into classical fluid dynamics.

In this work, we investigate dynamic similarity in the wake dynamics in a superfluid, focusing on a regime involving a *penetrable* obstacle. The feature by which the fluid can penetrate the body of the obstacle fundamentally modifies the vortex nucleation process [20, 29]. In contrast to impenetrable hard obstacles, which nucleate individual vortices from the boundary of density-depleted regions, penetrable obstacles produce vortex dipoles through a precursor rarefaction pulse. This penetrable obstacle constitutes a regime without a true classical analogue, but it is readily realized in atomic Bose-Einstein condensate (BEC) experiments using a focused laser beam whose potential strength imparted onto the atoms is below the chemical potential of the BEC [20, 27, 29–31]. There have been experimental studies of penetrable obstacles in which the periodic generation of vortex dipoles from a moving obstacle was observed [29] and the quantitative relationship between the dipole generation rate and the obstacle speed and strength was investigated [27]. Because the dynamic similarity in wake dynamics was numerically presented for impenetrable obstacles [25], it is highly desirable to extend this concept to penetrable obstacles. However, a unifying quantitative framework for vortex shedding across

* yishin@snu.ac.kr

different regimes is still lacking, particularly because it is difficult to define the length scale of the penetrable obstacle in an unambiguous manner.

Here, we analyze shedding dynamics from a penetrable obstacle by numerically solving Gross–Pitaevskii equations (GPEs) and present an appropriate *effective length scale* that captures the evolution of the shedding behaviors. We define the effective diameter from the Mach-1 contour of the time-averaged irrotational flow around the penetrable obstacle, which delineates the locally supersonic region where quantized vortices nucleate. We demonstrate that once this length is incorporated into a new superfluid Reynolds number, the resulting dimensionless quantities, in this case the Strouhal number and drag coefficient, exhibit universal behaviors in close analogy with classical fluids. Our findings thus extend the scope of dynamic similarity to penetrable superfluid flows, showing that even in this uniquely quantum regime, the universal language of fluid dynamics persists.

II. METHOD

We consider a situation in which a BEC flows at constant velocity $\mathbf{v}_\infty = -v_0\hat{\mathbf{x}}$ through obstacle potential $V(\mathbf{r})$. To simulate the superfluid vortex shedding induced by the obstacle, we numerically solve the two-dimensional GPE for the condensate wave function $\psi(\mathbf{r}, t)$, which is given by

$$i\hbar\frac{\partial\psi}{\partial t} = \left(-\frac{\hbar^2}{2m}\nabla^2 + i\hbar v_0\frac{\partial}{\partial x} + V(\mathbf{r}) + g|\psi|^2\right)\psi, \quad (1)$$

where m is the mass of the particles and g is the interaction strength. The wave function can be expressed as $\psi(\mathbf{r}, t) = \sqrt{\rho(\mathbf{r}, t)}e^{i\theta(\mathbf{r}, t)}$, where ρ and θ denote the density and phase of the condensate, respectively, and the local superfluid velocity is expressed as $\mathbf{v}(\mathbf{r}, t) = (\hbar/m)\nabla\theta$. The obstacle is modeled by Gaussian potential $V(\mathbf{r}) = V_0 \exp[-2(x^2 + y^2)/\sigma^2]$, where $V_0(> 0)$ is the peak barrier height and σ is the $1/e^2$ radius. For a penetrable obstacle, we take $V_0 < \mu$, where $\mu = g\rho_0$ is the chemical potential of the condensate, such that no fully depleted density core forms, in contrast to the impenetrable case [20].

The initial trial wavefunction was prepared from the Thomas–Fermi approximation in the presence of the obstacle and relaxed to the true ground state for a stationary BEC by imaginary-time propagation [32]. The real time evolution is calculated using the Fourier pseudo-spectral method [33] with the fourth order Runge–Kutta method with $\Delta t = 0.01\tau$ and $\tau = \hbar/\mu$. During real-time evolution, the background flow was linearly increased to target velocity v_0 over a short acceleration interval of 0.1τ . The simulation domain is $-350 < x/\xi < 150$ and $|y/\xi| < 125$ and the spatial resolution is 0.5ξ per grid point, where $\xi = \hbar/\sqrt{m\mu}$ is the condensate healing length.

To track the long-time evolution until the wake pattern reaches a steady state, we utilize the fringe region technique [25, 34] in the edge region of the computational domain. The fringe region serves to absorb the propagating density undulation, preventing interference from waves. This is implemented with damping function $\gamma(\mathbf{r})$. We set $\gamma(\mathbf{r}) = \max[\gamma(x), \gamma(y)]$, where

$$\gamma(\alpha) = \frac{\gamma_0}{2} \left\{ 2 + \tanh\left(\frac{\alpha - w_\alpha}{d}\right) - \tanh\left(\frac{\alpha + w_\alpha}{d}\right) \right\}, \quad (2)$$

with $\alpha = x, y$, $\gamma_0 = 0.1$, $w_x = 25\xi$, $w_y = 20\xi$ and $d = 3\xi$. Furthermore, to prevent vortex reentry under the periodic boundary conditions, we use the vortex unwind algorithm to remove the vortex adjacent to the boundary region [25, 35]. Vortex removal is implemented every 5τ during time evolution.

To investigate the steady situation, we examined the vortex shedding over a window of $2000\tau \leq t \leq 10000\tau$, thus excluding the initial acceleration stage. To break symmetry during initial shedding, we added a small amount of complex random noise to the initial field after the imaginary time evolution, with uniformly distributed real and imaginary parts scaled to a relative amplitude of the order of 10^{-4} .

III. RESULTS

A. Vortex dipole–to–cluster transition

To characterize the shedding behavior for a penetrable obstacle, we evaluated two quantities from numerical simulations: the spatial distribution of superfluid vorticity $\omega_s(\mathbf{r})$ and the temporal evolution of the force $\mathbf{F}(t)$ exerted by the obstacle potential. The superfluid vorticity is defined as the curl of the supercurrent density [37],

$$\omega_s = \frac{1}{2}\nabla \times (\rho\mathbf{v}) = \frac{1}{2i}(\partial_x\psi^*\partial_y\psi - \partial_y\psi^*\partial_x\psi), \quad (3)$$

providing a convenient measure of vortex generation, annihilation, and propagation around the obstacle. The force by the obstacle is, according to Ehrenfest’s theorem, estimated as

$$\mathbf{F}(t) = -\iint_{\Omega} dx dy |\psi(\mathbf{r}, t)|^2 \nabla \left[\frac{V(\mathbf{r}, t)}{m} \right], \quad (4)$$

where Ω is the two-dimensional computational domain. The force is decomposed as $\mathbf{F}(t) = F_D(t)\hat{\mathbf{x}} + F_L(t)\hat{\mathbf{y}}$, where F_D and F_L are the drag and lift components, parallel and perpendicular to the background flow, respectively.

In Fig. 1, we display $\omega_s(\mathbf{r})$ and $\mathbf{F}(t)$ for different flow velocities with $V_0/\mu = 0.9$ and $\sigma/\xi = 20$. Just above the critical velocity $v_c \approx 0.18c_{s0}$, where $c_{s0} = \sqrt{\mu/m}$ is the speed of sound in the unperturbed condensate, vortex dipoles are nucleated within the penetrable obstacle via

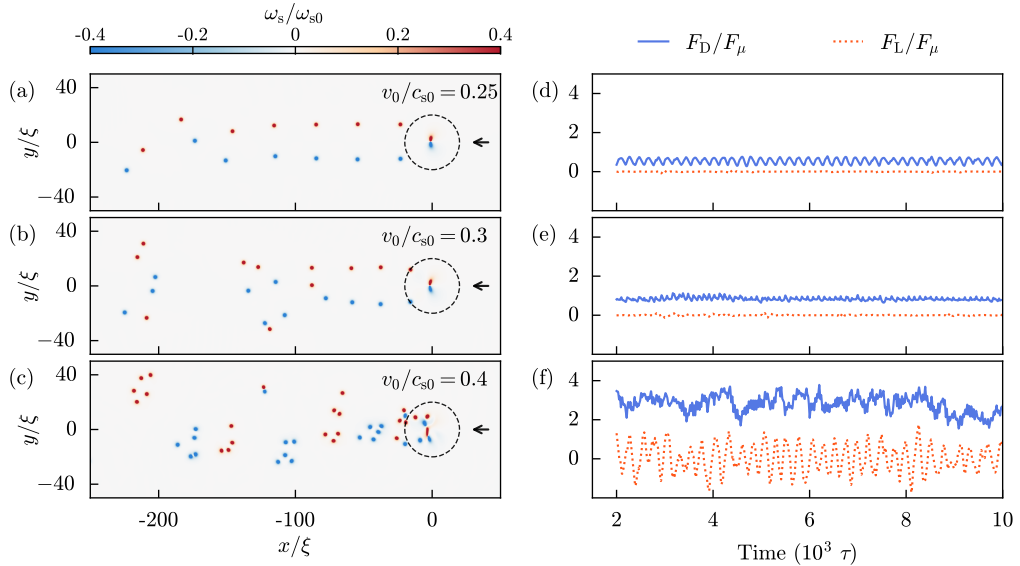


FIG. 1. Vortex shedding in a Bose-Einstein condensate flowing past a penetrable obstacle. The condensate flows from right to left (black arrow) at a speed of v_0 . The Gaussian obstacle has strength $V_0/\mu = 0.9$ and width $\sigma/\xi = 20$. (a)–(c) Superfluid vorticity distributions $\omega_s(\mathbf{r})$ for $v_0/c_{s0} = 0.25$ (a), 0.30 (b), and 0.40 (c), where c_{s0} is the speed of sound in the unperturbed condensate. $\omega_s(\mathbf{r})$ is normalized by $\omega_{s0} = \rho_0/\tau$. As v_0 increases, shedding evolves from periodic vortex-dipole emission to same-signed vortex-cluster shedding. Dashed circles indicate the obstacle's $1/e^2$ radius, centered at $x = 0$. (d)–(f) Time traces of drag force F_D (solid blue) and lift force F_L (dotted red) for the same parameters used in (a)–(c). The force is normalized by $F_\mu = \mu/\xi$. With an increase in v_0 , F_D grows and becomes irregular, while F_L increases in terms of its magnitude and oscillatory strength, reflecting the transition from dipole- to cluster-dominated shedding.

phase accumulation and phase slip (Fig. 1(a)) [20]. These dipoles form nearly parallel rows as they propagate downstream. Because such dipole rows are intrinsically unstable [38], the downstream wake gradually reorganizes into a staggered V-shaped pattern [21]. As the velocity increases, this instability spreads upstream toward the obstacle, resulting in increasingly irregular vortex configurations in the near wake (Fig. 1(b)). At still higher velocities, the nucleation mechanism itself becomes unstable, exhibiting a qualitative change (Fig. 1(c)): rarefaction pulses fragment into multiple vortices, which subsequently interact, annihilate, or produce Jones–Roberts solitons [39]. These interactions lead to the formation of same-sign vortex clusters that persist downstream and may eventually organize into a quasi–von Kármán street [40], despite the fact that the obstacle is penetrable.

The corresponding force response, shown in Figs. 1(d)–1(f), reflects the same progression. In the dipole–row regime near v_c , the drag force exhibits periodic oscillations with negligible lift, consistent with symmetric dipole nucleation. As the velocity increases, the drag oscillation frequency rises and the signal fluctuates slightly more, in line with the growing instability in the wake. Once vortex clusters appear, the drag force becomes strongly irregular, while the lift force develops pronounced periodic oscillations associated with alternating cluster formation (Fig. 1(f)). It is clearly revealed that the shedding behavior for a penetrable obstacle

changes from periodic dipole–row emission to alternating same–sign vortex cluster shedding as the flow velocity increases, which is consistent with earlier numerical studies [41].

We investigate the dipole–to–cluster transition further by examining the velocity dependence of the drag and lift forces. Fig. 2(a) shows the time-averaged drag force $\overline{F_D}$ and the root-mean-square of the lift force, $(\overline{F_L^2})^{1/2}$ as functions of v_0 . Here, the time averages are evaluated for $2000 \leq t/\tau \leq 10000$ with snapshots sampled every $\Delta t = 10\tau$. Both the drag and lift exhibit sudden increases at threshold velocity $v_{th} \simeq 0.33 c_{s0}$, which is also associated with the onset of asymmetric vortex cluster shedding. Interestingly, we find that the drag force closely follows the scaling $\overline{F_D} \sim (v_0 - v_c)^{1/2}$ in the low-velocity dipole-emission regime [42], while it evolves to quadratic dependence $\overline{F_D} \sim (v_0 - v_c)^2$ in the high-velocity cluster-shedding regime (Fig. 2(a) inset).

The dipole–to–cluster transition is also examined by analyzing the oscillatory behavior of the drag and lift forces through their Fourier spectra. The drag force displays a well-defined shedding frequency up to v_{th} , consistent with the periodic dipole emission, while above v_{th} , the spectrum becomes irregular and no dominant frequency remains. In contrast, the lift force shows a negligible spectral weight below v_{th} but develops a clear oscillation frequency above v_{th} , reflecting the alternating release of vortex clusters. From the spectral peaks of the Fourier spectra of $F_D(t)$ and $F_L(t)$, we determine their character-

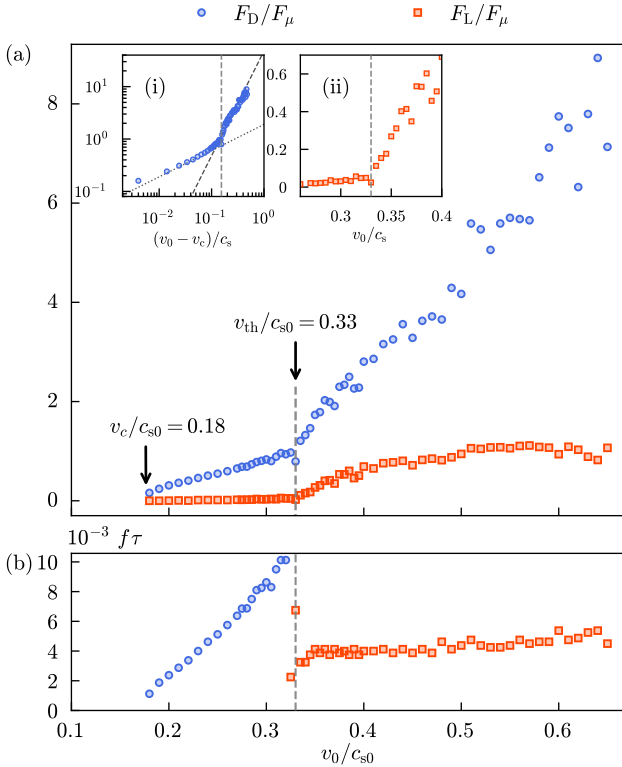


FIG. 2. Drag and lift responses for a penetrable obstacle with $V_0/\mu = 0.9$ and $\sigma/\xi = 20$. (a) Mean drag \overline{F}_D (blue circles) and the root-mean-square of the lift $(\overline{F}_L^2)^{1/2}$ (red squares) versus background flow speed v_0/c_{s0} . The critical velocity $v_c = 0.18c_{s0}$ and the dipole-to-cluster transition velocity $v_{th} = 0.33c_{s0}$ are indicated by the black arrow and the grey dashed line, respectively. Left inset: log-log plot of F_D versus $(v_0 - v_c)$ with guide lines $(v_0 - v_c)^{1/2}$ (dotted) and $(v_0 - v_c)^2$ (dashed). Right inset: magnified view of F_L near the transition, showing a rapid rise for $v_0 > v_{th}$. (b) Drag and lift frequencies f_D and f_L as functions of v_0/c_{s0} . The frequencies are normalized by $1/\tau = \mu/\hbar$. Reliable determinations were obtained for f_D when $v_0 < v_{th}$ and for f_L when $v_0 > v_{th}$.

istic oscillating frequencies f_D and f_L , respectively. The measurement results are shown in Fig. 2(b) for the corresponding shedding regimes across the threshold velocity. In the dipole shedding regime, f_D increases almost linearly with an increase of v_0 above v_c , consistent with previous experiments [27, 29] and in the cluster shedding regime, on the other hand, f_L exhibits very weak dependence on v_0 . Upon crossing the threshold velocity v_{th} , the measured frequencies suggest a relationship of $f_L \approx f_D/2$, which is understandable with the fact that a vortex cluster consists of same-sign vortices.

B. Effective Diameter

Our analysis of the wake morphology and force response clearly shows a distinct dipole-to-cluster transition in the superfluid shedding dynamics for a pen-

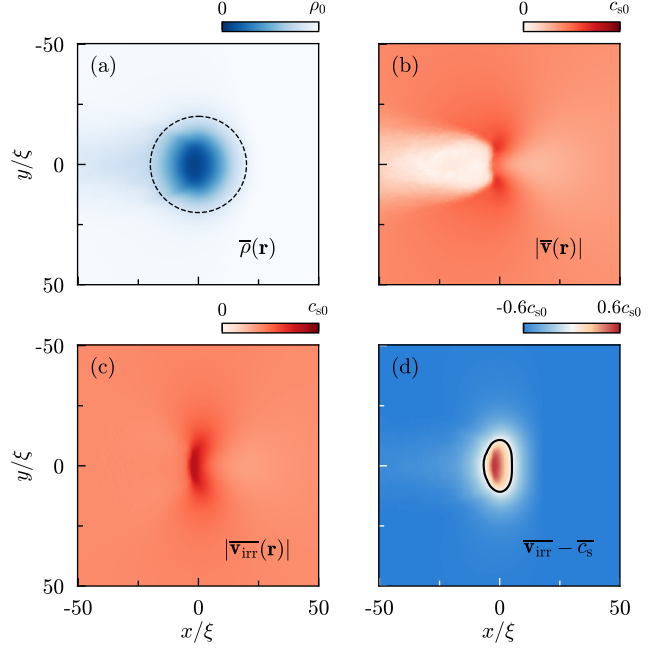


FIG. 3. Time-averaged flow fields around a penetrable obstacle for $V_0/\mu = 0.9$, $\sigma/\xi = 20$, and $v_0/c_{s0} = 0.4$. (a) Condensate density $\overline{\rho}(\mathbf{r})$; the dashed circle indicates the obstacle's $1/e^2$ radius. (b) Flow speed $|\overline{\mathbf{v}}(\mathbf{r})|$ and (c) irrotational flow speed $|\overline{\mathbf{v}}_{\text{irr}}(\mathbf{r})|$. (d) Difference $|\overline{\mathbf{v}}_{\text{irr}}(\mathbf{r})| - \overline{c_s}(\mathbf{r})$, where $\overline{c_s}(\mathbf{r})$ is the local speed of sound as determined by $\overline{\rho}(\mathbf{r})$. The black contour is the Mach-1 locus $|\overline{\mathbf{v}}_{\text{irr}}(\mathbf{r})| = \overline{c_s}(\mathbf{r})$.

trable obstacle. In this section, we introduce the *effective diameter* D_{eff} for a penetrable obstacle to determine the characteristic length scale relevant to the shedding dynamics, which would allow one to define a proper superfluid Reynolds number Re_s to organize the shedding behavior within the framework of dynamic similarity.

The nucleation of vortices in a superfluid occurs, in general, once compressibility effects become unstable [43–47]. This condition is referred to as the local Landau criterion and is expressed as

$$v(\mathbf{r}) > c_s(\mathbf{r}) = \sqrt{g\rho(\mathbf{r})/m}, \quad (5)$$

where $c_s(\mathbf{r})$ denotes the local speed of sound. This proposes that the spatial region around the obstacle where the flow becomes locally supersonic can be considered as the effective spatial extent of the obstacle in terms of vortex shedding. We thus define the effective obstacle diameter D_{eff} as the transverse width of the locally supersonic region (along the y -direction).

To gain insight into the flow structure around a penetrable obstacle, we examine the spatial distributions averaged over time of the density $\overline{\rho}(\mathbf{r})$ and velocity $\overline{\mathbf{v}}(\mathbf{r})$. The exemplary data in the case of $v_0 > v_{th}$ are shown in Fig. 3. The density of condensate $\overline{\rho}$ exhibits a slight suppression compared to that of a stationary flow behind the obstacle due to the trail of the shed vortices downstream (Fig. 3(a)). The average flow speed $|\overline{\mathbf{v}}|$ in Fig. 3(b) clearly

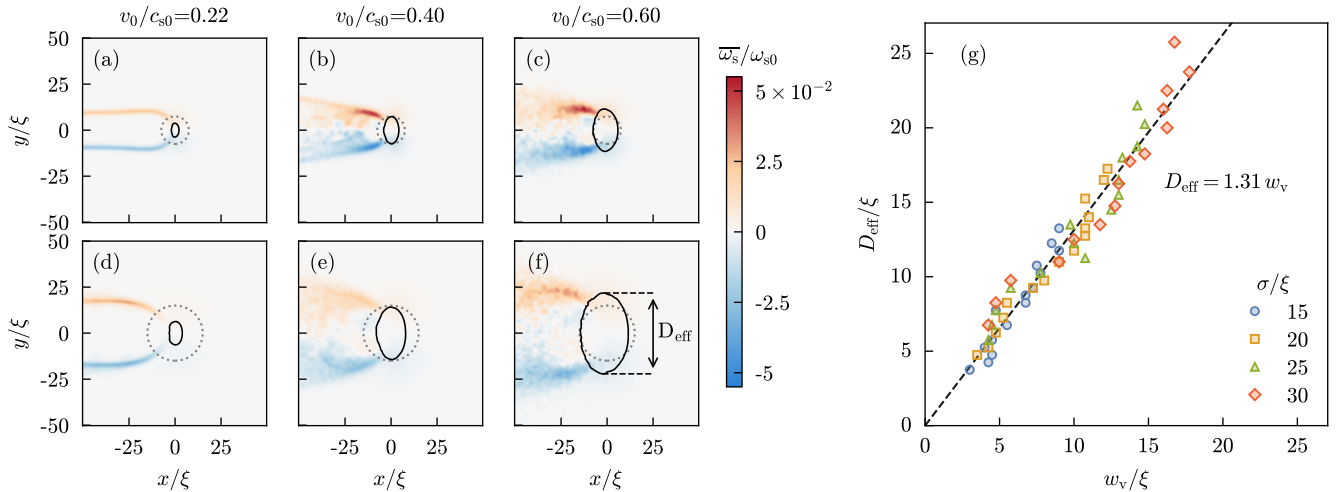


FIG. 4. Time-averaged vorticity fields $\bar{\omega}_s(\mathbf{r})$ for various flow speeds v_0/c_{s0} ; (a-c) $V_0/\mu = 0.9$ and $\sigma/\xi = 20$, and (d-f) $V_0/\mu = 0.9$ and $\sigma/\xi = 40$. The black solid contour denotes the Mach-1 locus $\bar{v}_{\text{irr}}(\mathbf{r}) = \bar{c}_s(\mathbf{r})$, enclosing the locally supersonic region, and the gray dotted circle marks the obstacle's $1/c^2$ radius. The effective distance D_{eff} is defined as the maximum extent of the Mach-1 region along the y direction. (g) Effective diameter D_{eff}/ξ versus vorticity width w_v/ξ . The width w_v was determined from $\bar{\omega}_s(\mathbf{r})$ (see text). Data points are shown for various values of σ and $0.22 \leq v_0/c_{s0} \leq 0.65$ at $V_0/\mu = 0.9$. Error bars are smaller than the symbols. The dashed line is a linear fit to the data.

reflects the influence of these vortices: downstream of the obstacle, a low-velocity region develops where the background flow is partially canceled by the vortex-induced flow, while on the upstream side of the obstacle center the flow velocity is locally enhanced.

Given that we are interested in determining the supersonic region *before* vortex shedding, it is desirable to estimate the velocity field without the chaotic wake induced by shed vortices. This can be done by calculating the compressible (irrotational) component of the velocity field $\mathbf{v}_{\text{irr}}(\mathbf{r})$ [23, 25, 44]. According to Helmholtz decomposition, $\mathbf{v} = \mathbf{v}_{\text{irr}} + \mathbf{v}_{\text{sol}}$ with $\nabla \times \mathbf{v}_{\text{irr}} = 0$ and $\nabla \cdot \mathbf{v}_{\text{sol}} = 0$. Because the contribution from vortices is isolated in the solenoidal component \mathbf{v}_{sol} , \mathbf{v}_{irr} cleanly separates the compressibility-driven instability from vortex-induced fluctuations. Because vortex nucleation is triggered by compressibility-related instabilities, it is physically more relevant to base D_{eff} on the compressible component.

In Fig. 3(c), we observe that the time-averaged irrotational flow speed reaches its maximum at the obstacle center. This means that phase slips caused by vortex nucleation, which relax the accumulated phase gradient, lead to an overall reduction of $|\mathbf{v}(\mathbf{r})|$ as shown in Fig. 3(b). Consequently, we define the relevant supersonic region as

$$\mathcal{S} \equiv \{\mathbf{r} \in \Omega : |\bar{v}_{\text{irr}}(\mathbf{r})| \geq \bar{c}_s(\mathbf{r})\}, \quad (6)$$

with $\bar{c}_s(\mathbf{r}) = \sqrt{g\rho(\mathbf{r})/m}$ and determine D_{eff} to be the transverse extent of \mathcal{S} through the obstacle center. In other words, D_{eff} corresponds to the transverse size of the Mach-1 contour around the obstacle (black solid line in Fig. 3(d)).

To test whether the supersonic region identified

through \bar{v}_{irr} suitably represents the vortex nucleation region, we compare it with the spatial distribution of the vortices. Figs. 4(a)–4(f) show the vorticity field averaged over time, $\bar{\omega}_s(\mathbf{r})$, together with the supersonic region defined by Eq. (6). Trails of positive (blue) and negative (red) vorticity appear just downstream of the obstacle. As the velocity increases, the vorticity-concentrated region expands and the vortex trail behind the obstacle grows into an enlarged wake along with the expansion of the supersonic region. $\bar{\omega}_s$ is predominantly concentrated along the lateral boundaries of the supersonic zone [63], in contrast to the fixed Gaussian width of the obstacle.

In Fig. 4(g), we plot the effective diameter D_{eff} for various Gaussian widths σ and flow speed v_0 compared to the lateral width w_v of the distribution $\bar{\omega}_s(\mathbf{r})$. Here, w_v is obtained by integrating $\bar{\omega}_s(\mathbf{r})$ along the x -direction within a finite region that encompasses the supersonic zone and extends downstream by 20ξ and by then determining the distance between the positive and negative peaks in the projected ω_s profile. The effective diameter shows a linear relationship with w_v , $D_{\text{eff}} \approx 1.31 w_v$, for a wide range of obstacle conditions. This shows that the supersonic region is the relevant length scale of the penetrable obstacle for vortex shedding. An analytical description of the v_0 -dependence of D_{eff} is presented in Appendix A.

From this observation and motivated by Reeve et al. [25], we propose a superfluid Reynolds number for penetrable obstacles, as follows:

$$\text{Re}_s = \frac{(v_0 - v_c)D_{\text{eff}}}{\hbar/m}. \quad (7)$$

In computing Re_s , we determined the critical velocity

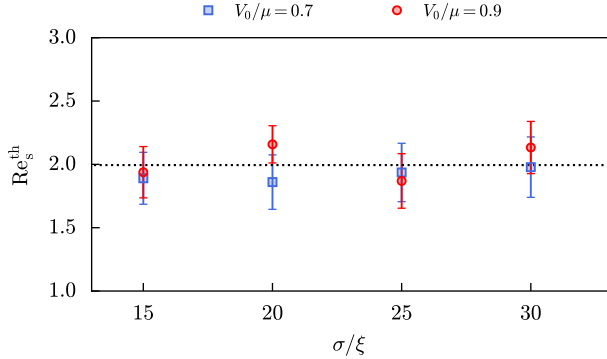


FIG. 5. Dynamic similarity of the dipole-to-cluster transition. Threshold superfluid Reynolds number Re_s^{th} at $v_0 = v_{\text{th}}$ for obstacle parameters $V_0/\mu \in \{0.7, 0.9\}$ and $\sigma/\xi \in \{15, 20, 25, 30\}$. Error bars indicate the uncertainties of Re_s^{th} , arising from the finite numerical resolution in determining v_c , v_{th} and D_{eff} . The black dotted line indicates the mean value of all data points.

v_c , following Refs. [20, 42], by using the imaginary-time propagation method to check the existence of a stationary ground-state solution for $v_0 < v_c$.

C. Superfluid Reynolds number Re_s and Strouhal number St

First, we examine whether the superfluid Reynolds number Re_s can serve as a reliable indicator of the dipole-to-cluster transition. In Fig. 5, we plot the values of Re_s^{th} at $v_0 = v_{\text{th}}$ for various obstacle conditions in terms of σ and V_0/μ . Here, v_{th} is determined as the velocity above which the drag force spectrum no longer shows a peak structure, which is fully correlated with the onset behavior of the lift force. It is remarkable that the dipole-to-cluster transition occurs consistently at $Re_s \approx 2$. This shows that the superfluid Reynolds number defined in Eq. (7) conveys the dynamic similarity in the wake dynamics for penetrable obstacles. We note that as the Gaussian width σ increases from 15ξ to 30ξ , the ratio of D_{eff}/σ decreases by a factor of 1.6, thus manifesting the efficacy of D_{eff} in representing the length scale of the obstacle.

Next, we examine the relationship between Re_s and the Strouhal number St for penetrable obstacles. Using the effective diameter, we compute St as follows:

$$St = \frac{f_s D_{\text{eff}}}{v_0}. \quad (8)$$

Here, the vortex shedding frequency f_s is determined via

$$f_s(v_0) = \begin{cases} f_L, & v_0 \geq v_{\text{th}}, \\ \frac{1}{2} f_D, & v_0 < v_{\text{th}}. \end{cases} \quad (9)$$

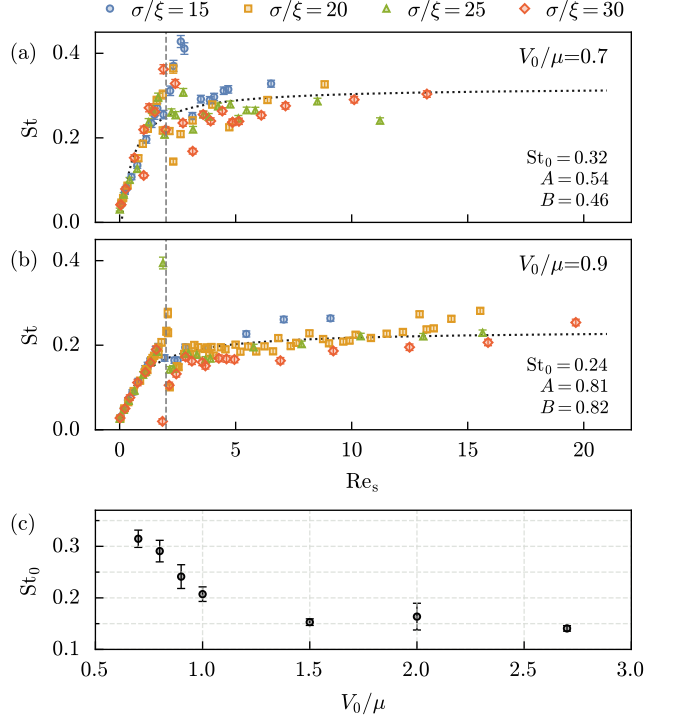


FIG. 6. Strouhal number St versus Re_s for $V_0/\mu = 0.7$ (a) and 0.9 (b). St was computed using D_{eff} [Eq. (8)]. Vertical dashed lines denote the dipole-to-cluster transition ($Re_s = 2$). Dotted curves are fits to $St(Re_s) = St_0 \left[1 - \frac{A}{Re_s + B} \right]$; fit parameters are listed in each panel. Error bars represent the uncertainty in St from the finite numerical resolution in determining D_{eff} and the FFT frequency resolution to extract f_s . (c) Asymptotic Strouhal number St_0 as a function of V_0/μ . St_0 was obtained by averaging St over $0.55 \leq v_0/c_{s0} \leq 0.65$ where St is saturated ($\sigma/\xi = 20$), and its error bar indicates the standard error of the mean.

For $v_0 < v_{\text{th}}$, the lift spectrum lacks a clear dominant peak; thus, we approximate f_s as half the drag frequency. This approach is motivated by the classical low-Re result showing that the lift frequency is half the drag frequency [48], and is supported by earlier studies of impenetrable obstacles [17, 21].

Figs 6(a) and 6(b) present our numerical results for $V_0/\mu = 0.7$ and 0.9 , respectively, on the plane of Re_s and St . For a fixed obstacle strength V_0/μ , data points of various obstacle sizes collapse onto a single curve. Moreover, we observe that St remains nearly constant for $Re_s > 2$, representing a close analogy to the classical case where St saturates in the turbulent vortex shedding regime [4]. The Re_s - St trend is well described by the empirical fit [2, 25]

$$St(Re_s) = St_0 \left[1 - \frac{A}{Re_s + B} \right], \quad (10)$$

which closely resembles the classical formulation. Within the limit of $Re_s \gg 1$, St asymptotically approaches $St_0 \simeq 0.20\text{--}0.30$, remarkably close to the classical value of $St_0 \simeq 0.21$ [2, 4].

To understand how St_0 depends on the obstacle strength, we extend our analysis across a wide range of barrier heights, including the impenetrable regime where D_{eff} remains well-defined. As shown in Fig. 6(c), St_0 gradually decreases from about 0.30 at $V_0/\mu = 0.7$ to around 0.15 at $V_0/\mu = 1.5$. Beyond this point, deeper in the impenetrable regime, St_0 remains nearly constant at ~ 0.15 , consistent with previous findings where the geometric obstacle diameter was used [25].

The systematic increase of St_0 with a decrease of V_0/μ in the penetrable regime likely reflects the decreasing robustness of vortex clustering for weaker obstacles. Because the value of St characterizes the geometric spacing of vortex clusters in the wake, larger values of St correspond to shorter inter-cluster distances ($\approx v_0/(2f_s)$). This leads to stronger overlaps between successive vortices with a finite core size, suppressing the formation of a stable vortex street. In our simulations, a well-defined shedding frequency ceases to appear for $V_0/\mu < 0.6$, consistent with previous observations [41].

D. Drag force

Finally, we investigate the dynamic similarity of the drag force for a penetrable obstacle. Following Ref. [26] and replacing the geometric diameter D with the effective diameter D_{eff} , we introduce the superfluid drag coefficient for a penetrable obstacle as

$$C_D \equiv \frac{2 \overline{F_D}}{\rho_0 (v_0^2 - v_c^2) D_{\text{eff}}}. \quad (11)$$

We note that this particular choice of drag coefficient is not unique [49].

In Fig. 7, we display the measured values of C_D as a function of Re_s . For a fixed obstacle strength V_0/μ , data obtained for different values of σ/ξ collapse onto a single curve, demonstrating dynamic similarity. At $Re_s \approx 2$, the drag coefficient curve exhibits characteristic bending that is nearly independent of σ/ξ . This feature is associated with the dipole-to-cluster transition.

To quantify the dependence of C_D on Re_s , we fit a power-law function of $C_D = b Re_s^{-\alpha}$ to the data for the two different ranges, $Re_s < 2$ and $Re_s \geq 2$, separately (Fig. 7 insets). For the low- Re_s dipole shedding regime, the exponent obtained is in the range of $\alpha = 0.6 \sim 0.7$, similar with Stokes' law in the 2D cylinder case in classical fluid dynamics [50, 51]. For the high- Re cluster shedding regime, the exponent decreases to $\alpha = 0.22 \sim 0.27$. Although C_D gradually decreases with an increase of Re_s in our parameter range, it is not known whether it vanishes as $Re_s \rightarrow \infty$. In classical fluids, it has been argued that the dissipation rate remains finite as $Re \rightarrow \infty$, implying a nonvanishing drag coefficient. However, studies under smooth wall or periodic boundary conditions have shown that the dissipation rate can decrease with an increase of Re [52, 53], suggesting that the drag coefficient

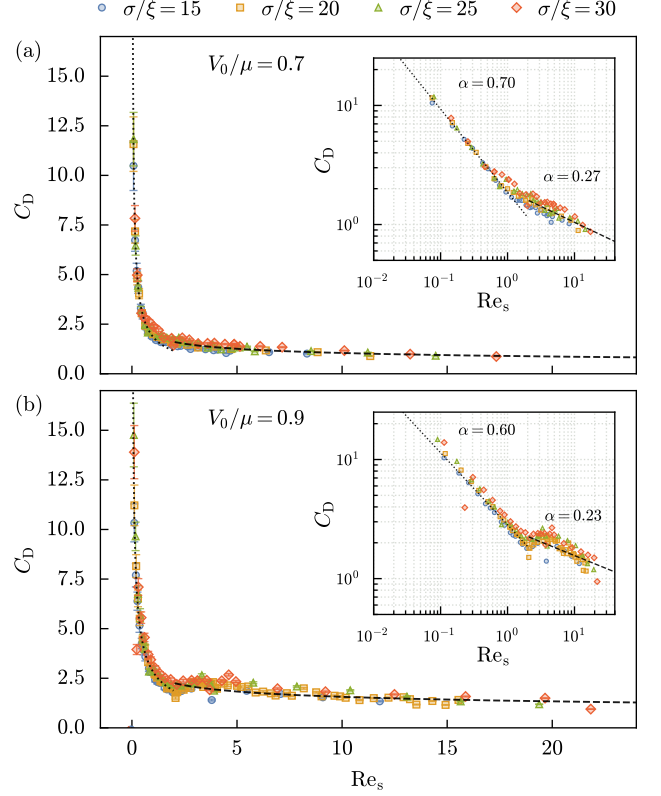


FIG. 7. Drag coefficient C_D for a penetrable obstacle as a function of Re_s . C_D was estimated via Eq. (11). (a,b) Numerical data for $V_0/\mu = 0.7$ (a) and 0.9 (b). The dashed (dotted) curve is a fit to $C_D = b Re_s^{-\alpha}$ for $Re_s \geq 2$ ($Re_s \leq 2$). Error bars represent the uncertainties of C_D , arising from the finite numerical resolution in the determination of v_c and D_{eff} . The insets display the same data on log-log axes, with fitted power-law exponents α .

may vanish. How this would be transformed in superfluid systems without intrinsic viscosity would be an interesting problem.

IV. CONCLUSION AND OUTLOOK

We have shown that vortex shedding past a penetrable obstacle in a two-dimensional superfluid can be organized by a flow-defined length scale, the effective diameter D_{eff} . Defined as the transverse extent of the region where the compressible component of the superflow exceeds the local speed of sound, D_{eff} delineates the Mach-1 contour that marks the onset of compressibility-driven instability. D_{eff} expands with v_0 and quantitatively matches the observed width of the vorticity distribution, confirming that the dynamically relevant scale is that felt by the flow rather than the geometric obstacle size. When forces and frequencies are normalized by D_{eff} , the Strouhal and drag coefficients collapse onto universal curves versus the superfluid Reynolds number Re_s , with a clear transition at

$\text{Re}_s \approx 2$. Thus, D_{eff} provides a unified similarity length governing both the shedding dynamics and mean dissipation in penetrable obstacle flows. This finding provides a basis for extending the universality observed in classical fluid dynamics to regimes beyond any classical counterpart.

We have also examined the cases of impenetrable obstacles and non-Gaussian penetrable obstacles, showing that qualitative behaviors remain consistent with the present universal trend (see Appendix C). These results indicate that the effective-diameter framework can extend to a broader class of flow geometries beyond simple Gaussian profiles. However, it should be noted that the present framework, based on the existence of a supersonic interface defined by the Mach-1 contour, cannot be applied to cases with higher drive velocities $v_0/c_{s0} > 1$, as the entire flow field becomes supersonic and no bounded nucleation zone can be identified. In the fully supersonic regime, dissipation is expected to be governed by different dynamical mechanisms such as shock waves rather than vortex shedding [30, 55, 57], implying the need for a different characteristic length scale. In classical compressible flows, the shock layer sets the pressure drag for flow past a bluff body [56], indicating that a scale based on the shock layer is a natural choice in this limit.

Finally, we note that the universality revealed here can be verified experimentally. The shedding frequency or St can be measured directly using a conventional time-of-flight image, as shown in Refs. [19, 27, 29]. In addition, the drag force can be measured without direct mechanical probes using a control-volume analysis, as suggested in Ref. [26]. Moreover, a recent proposal based on matter wave optics [58] suggests that both the superfluid velocity fields and the phase of the order parameter can be measured using phase-imprinting techniques [59–61], making it feasible to visualize the Mach-1 contour and measure D_{eff} directly. Such experimental methods would allow testing the predicted universal behaviors.

V. ACKNOWLEDGEMENTS

We thank Haneul Kwak for providing the simulation code, Myeonghyeon Kim for computing server support, and J. Park, D. Bae, J. Lee, S. Kim, and J. Jung for their insightful discussions. This work was supported by the National Research Foundation of Korea (Grants No. RS-2023-NR077280, No. RS-2023-NR119928, and No. RS-2024-00413957).

APPENDIX A: DEPENDENCE OF D_{eff} ON v_0

We consider steady flow past a Gaussian obstacle within a first-order perturbative potential-flow framework. In the stationary regime, and neglecting the quantum pressure term, the GPE takes a Bernoulli-like form,

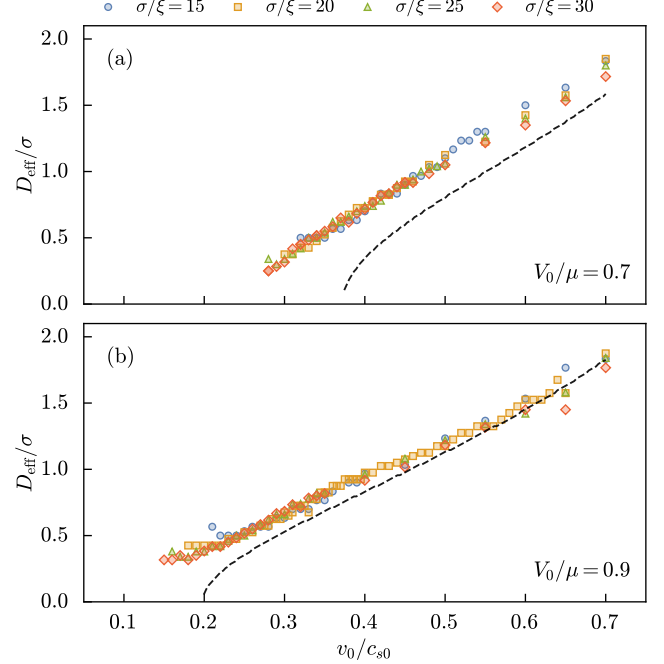


FIG. 8. Flow-speed dependence of D_{eff} . D_{eff}/σ as a function of v_0/c_{s0} for different Gaussian widths σ at $V_0/\mu = 0.7$ (a) and 0.9 (b). Error bars are smaller than the symbols. Dashed lines show theoretical estimates from a perturbative steady-flow model using Eq. (15).

$$g\rho(r) + V(r) + \frac{1}{2}mv(r)^2 = g\rho_0 + \frac{1}{2}mv_0^2, \quad (12a)$$

$$\nabla \cdot [\rho(r)v(r)] = 0. \quad (12b)$$

We examine small deviations around a uniform background flow,

$$\mathbf{v}(\mathbf{r}) = -v_0 \hat{\mathbf{x}} + \frac{\hbar}{m} \nabla \phi(\mathbf{r}), \quad (13a)$$

$$\rho(\mathbf{r}) = \rho_0 + \delta\rho(\mathbf{r}), \quad (13b)$$

with $|\frac{\hbar}{m} \nabla \phi| \ll v_0$ and $|\delta\rho| \ll \rho_0$. Substituting Eq. (13) into Eq. (12) and retaining only terms linear in v_0/c_{s0} yields the Poisson equation,

$$\partial_x^2 \phi(\mathbf{r}) + \partial_y^2 \phi(\mathbf{r}) = -\frac{v_0}{\hbar c_{s0}^2} \partial_x V(\mathbf{r}). \quad (14)$$

For a Gaussian obstacle $V(\mathbf{r}) = V_0 \exp(-2r^2/\sigma^2)$, the solution for Eq. (14) is given by

$$\phi(\mathbf{r}) = -V_0 \frac{v_0}{4\hbar c_{s0}^2} \sigma^2 \frac{\cos \theta}{r} \left[1 - \exp\left(-\frac{2r^2}{\sigma^2}\right) \right]. \quad (15)$$

Combining Eq. (12) and Eq. (13) gives the local flow speed and density up to linear order in v_0/c_{s0} ,

$$|\mathbf{v}|^2 = v_0^2 - \frac{2\hbar}{m} v_0 \partial_x \phi, \quad \rho = \rho_0 - \frac{V}{g} + \frac{\hbar}{g} v_0 \partial_x \phi. \quad (16)$$

Using Eq. (15), we obtain

$$\frac{\hbar}{m} \partial_x \phi = \frac{V_0}{4mc_{s0}^2} v_0 \frac{\sigma^2}{r^2} \cos(2\theta). \quad (17)$$

Thus, the flow speed is enhanced and the density is reduced on the lateral sides of the obstacle ($\theta = \pm\pi/2$, $\cos 2\theta = -1$), while the opposite occurs along the flow axis ($\theta = 0$ or π , $\cos 2\theta = 1$). Consequently, as v_0 increases, the region satisfying the local supersonic condition, $|\mathbf{v}(\mathbf{r})| > c_s(\mathbf{r})$, expands preferentially in the transverse direction. This leads to a lateral widening of the Mach-1 contour and thus an increase in the effective diameter D_{eff} .

In Fig. 8, we compare the effective diameter obtained from this perturbative potential-flow solution with that extracted from full GPE simulations. The perturbative calculation captures, at a qualitative level, the increase of D_{eff} with v_0 . It also predicts a minimum velocity above which the supersonic region acquires a finite extent; this threshold exceeds the actual critical velocity v_c . The discrepancy is attributed to the neglect of higher-order corrections and of the quantum-pressure term, which plays a crucial role in triggering vortex shedding.

APPENDIX B: DIPOLE EMITTING FREQUENCY

In the vortex dipole regime for $\text{Re}_s < 2$, the emitting frequency f_D shows a linear relationship with the flow speed v_0 . This linearity was observed in previous experiments [27, 29], where a model of $f_D = a(v_0 - v_c)$ was suggested and employed to extract the critical velocity v_c . Furthermore, in Ref. [27], it was reported that the linear-response slope a increased with an increase in the strength V_0 of the penetrable obstacle.

In Fig. 9(a), we show our numerical results of f_D for different obstacle strengths with $\sigma/\xi = 20$. The drag frequency is well described by the linear relationship with v_0 , but the critical velocity is slightly higher than that determined by the linear extrapolation of the emitting frequency. Noticeably, the value a decreases with an increase of V_0 , which is in stark contrast to the experimental observation. We attribute this discrepancy to the finite-length driving protocol used in the experiments: the limited obstacle motion introduces acceleration phases and interactions between emitted vortices, which can affect the measured shedding frequency. We confirmed this interpretation with our various numerical simulations.

The relationship of $f_D = a(v_0 - v_c)$ suggests that the Strouhal number at $v_0 = v_{\text{th}}$ is given by

$$\text{St}_{\text{th}} = \frac{(f_D/2)D_{\text{eff}}}{v_{\text{th}}} = \frac{a(v_{\text{th}} - v_c)D_{\text{eff}}}{2v_{\text{th}}} \approx \frac{\hbar}{m} \frac{a}{v_{\text{th}}}, \quad (18)$$

where the last equality follows from $\text{Re}_s^{\text{th}} \approx 2$. The observation that both v_{th} and $\text{St}_{\text{th}} \sim \text{St}_0$ decrease with an

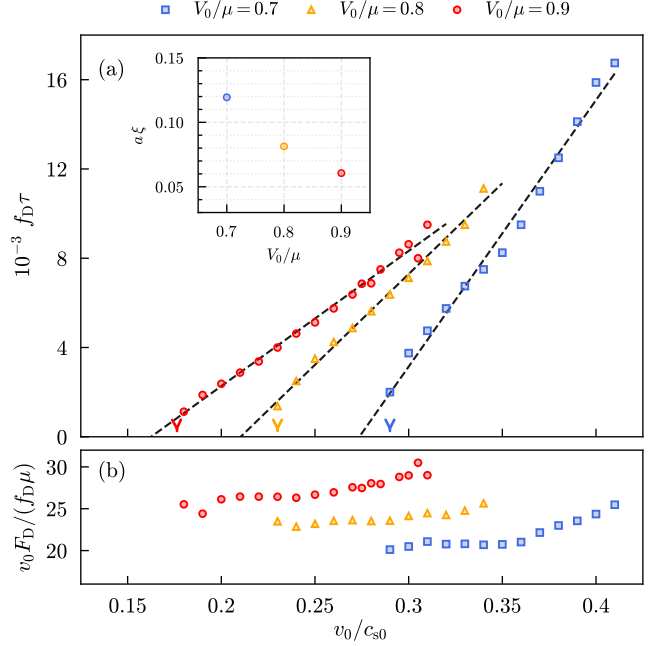


FIG. 9. Periodic vortex-dipole emission. (a) Drag frequency f_D as a function of v_0/c_{s0} for different values of V_0/μ with $\sigma/\xi = 20$. Dashed lines show the linear fits of $f_D = a(v_0 - v'_c)$ to the data sets with a and v'_c being the fitting parameters. The critical velocities v_c are indicated by color-matched wedge markers and are higher than v'_c . The inset shows the fitted values of a , normalized by $1/\xi$. (b) Estimated vortex-dipole energy $E_v = v_0 F_D / f_D$ [Eq. (19)]. The Energy is normalized by μ .

increase in V_0 is consistent with the dependence of a on V_0 .

In addition, we consider the energetics of the obstacle's drag effect in the dipole emission regime. The work done by the drag force on the fluid should be equal to the dissipated energy through vortex dipole nucleation, which is expressed as

$$F_D v_0 = E_v f_D, \quad (19)$$

where E_v is the energy cost of a vortex dipole. In Fig. 9(b), we show the variations of $E_v = v_0 F_D / f_D$ for different obstacle conditions. E_v increases steadily with the background flow speed v_0 . Since the energy of a pair of vortices of opposite-signs separated by D_{pair} is given by $E_v \propto \ln(D_{\text{pair}}/\xi)$, the increase in E_v implies that the separation D_{pair} increases with the velocity. This behavior is fully consistent with the v_0 -dependence of the effective obstacle diameter D_{eff} (Appendix A).

Together, the behaviors of $a(V_0)$, $v_0 F_D / f_D$, and $D_{\text{eff}}(v_0)$ provide a coherent description of the periodic vortex-dipole emission process.

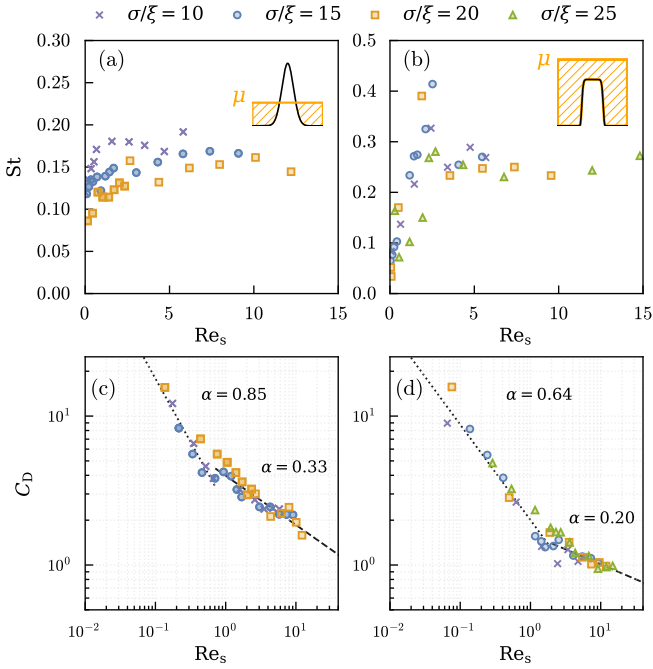


FIG. 10. St and C_D versus Re_s for impenetrable Gaussian obstacles (a,c) and penetrable super-Gaussian obstacles (b,d). Insets in (a) and (b) show the corresponding obstacle profiles relative to the chemical potential μ . Dashed(dotted) lines in (c) show fits to $C_D = b Re_s^{-\alpha}$ for $Re_s \geq 0.7$ ($Re_s \leq 0.7$). Similarly, the lines in (d) correspond to fits over $Re_s \geq 2$ ($Re_s \leq 2$).

APPENDIX C: EXTENSION TO DIFFERENT OBSTACLES

To test whether the effective diameter D_{eff} provides a unified description beyond penetrable Gaussian obstacles,

we repeated the St and C_D analysis using D_{eff} for two additional cases: an impenetrable Gaussian obstacle with $V_0/\mu = e$, and a penetrable super-Gaussian obstacle $V(\mathbf{r}) = V_0 \exp[-2(r/\sigma)^6]$ at $V_0/\mu = 0.7$ (Fig. 10). In both cases, St and C_D collapse versus Re_s constructed with D_{eff} .

For the impenetrable Gaussian obstacle (Figs. 10(a) and 10(c)), the shedding behavior and wake transition reproduce Ref. [25]: a von Kármán street of same-sign vortex pairs (K2 regime) for $Re_s < 0.7$, followed by irregular shedding beyond $Re_s \simeq 0.7$. For a consistent comparison with Ref. [26], we analyzed the drag coefficient by subtracting the large- Re_s asymptote, C_{D0} , rather than fitting C_D directly. This yields $C_{D0} = 2.06$, with power-law exponents $\alpha_1 = 1.37$ for $Re_s < 0.7$ and $\alpha_2 = 1.55$ for $Re_s > 0.7$. Compared with the results of $C_{D0} = 2.37$, $\alpha_1 = 1.06$ and $\alpha_2 = 0.72$ in Ref. [26], our exponents are larger, likely because we use the flow-defined D_{eff} , which increases with an increase of v_0 , rather than a fixed Thomas-Fermi zero-density size as the characteristic length.

For the penetrable super-Gaussian obstacle (Figs. 10(b) and 10(d)), whose top is flatter than a standard Gaussian, the shedding dynamics closely mirror those of the penetrable Gaussian: periodic dipole emission at lower Re_s values, evolving into irregular shedding with same-sign vortex clusters at higher Re_s values. These results support D_{eff} as a robust, obstacle-agnostic scale that organizes superfluid wake dynamics.

-
- [1] G. K. Batchelor, *An Introduction to Fluid Dynamics* (Cambridge University Press, England, 2000).
- [2] A. Roshko, On the development of turbulent wakes from vortex streets, National Advisory Committee for Aeronautics Technical Note 1191, California Institute of Technology, 1953.
- [3] M. Provansal, C. Mathis, and L. Boyer, Bénard–von Kármán instability: transient and forced regimes, *J. Fluid Mech.* **182**, 1 (1987).
- [4] J. H. Lienhard, Synopsis of lift, drag, and vortex frequency data for rigid circular cylinders, in *Technical Extension Service* (Washington State university, Bulletin, 1966).
- [5] A. Roshko, Experiments on the flow past a circular cylinder at very high Reynolds number, *J. Fluid Mech.* **10**, 345 (1961).
- [6] E. Berger and R. Wille, Periodic flow phenomena, *Annu. Rev. Fluid Mech.* **4**, 313 (1972).
- [7] H. Oertel Jr, Wakes behind blunt bodies, *Annu. Rev. Fluid Mech.* **22**, 539 (1990).
- [8] P. Kapitza, Viscosity of liquid helium below the λ -point, *Nature (London)* **141**, 74 (1938).
- [9] J. F. Allen and A. D. Misener, Flow phenomena in liquid helium II, *Nature (London)* **142**, 643 (1938).
- [10] G. W. Rayfield and F. Reif, Quantized vortex rings in superfluid helium, *Phys. Rev.* **136**, A1194 (1964).
- [11] L. D. Landau and E. M. Lifshitz, *Fluid Mechanics: Course of Theoretical Physics*, 2nd ed. (Elsevier, New York, 1987), Vol. 6.
- [12] A. Ramanathan, K. C. Wright, S. R. Muniz, M. Zeilan, W. T. Hill III, C. J. Lobb, K. Helmerson, W. D. Phillips, and G. K. Campbell, Superflow in a toroidal Bose–Einstein condensate: an atom circuit with a tunable weak link, *Phys. Rev. Lett.* **106**, 130401 (2011).
- [13] T. W. Neely, E. C. Samson, A. S. Bradley, M. J. Davis, and B. P. Anderson, Observation of vortex dipoles in an oblate Bose–Einstein condensate, *Phys. Rev. Lett.* **104**, 160401 (2010).

- [14] T. W. Neely, A. S. Bradley, E. C. Samson, S. J. Rooney, E. M. Wright, K. J. H. Law, R. Carretero-González, P. G. Kevrekidis, M. J. Davis, and B. P. Anderson, Characteristics of two-dimensional quantum turbulence in a compressible superfluid, *Phys. Rev. Lett.* **111**, 235301 (2013).
- [15] M. R. Matthews, B. P. Anderson, P. C. Haljan, D. S. Hall, C. E. Wieman, and E. A. Cornell, Vortices in a Bose–Einstein condensate, *Phys. Rev. Lett.* **83**, 2498 (1999).
- [16] C. Raman, M. Köhl, R. Onofrio, D. S. Durfee, C. E. Kuklewicz, Z. Hadzibabic, and W. Ketterle, Evidence for a critical velocity in a Bose–Einstein condensed gas, *Phys. Rev. Lett.* **83**, 2502 (1999).
- [17] K. Sasaki, N. Suzuki, and H. Saito, Bénard–von Kármán vortex street in a Bose–Einstein condensate, *Phys. Rev. Lett.* **104**, 150404 (2010).
- [18] G. W. Stagg, N. G. Parker, and C. F. Barenghi, Quantum analogues of classical wakes in Bose–Einstein condensates *J. Phys. B: At. Mol. Opt. Phys.* **47**, 095304 (2014).
- [19] W. J. Kwon, J. H. Kim, S. W. Seo, and Y. Shin, Observation of von Kármán vortex street in an atomic superfluid gas, *Phys. Rev. Lett.* **117**, 245301 (2016).
- [20] H. Kwak, J. H. Jung, and Y. Shin, Minimum critical velocity of a Gaussian obstacle in a Bose–Einstein condensate, *Phys. Rev. A* **107**, 023310 (2023).
- [21] X.-L. Li, X.-Y. Yang, N. Tang, L. Song, Z.-K. Zhou, J. Zhang, and Y.-R. Shi, Kármán vortex street in a two-component Bose–Einstein condensate, *New J. Phys.* **21**, 103046 (2019).
- [22] J. Maurer and P. Tabeling, Local investigation of superfluid turbulence, *Europhys. Lett.* **43**, 29 (1998).
- [23] N. Navon, A. L. Gaunt, R. P. Smith, and Z. Hadzibabic, Emergence of a turbulent cascade in a quantum gas, *Nature (London)* **539**, 72 (2016).
- [24] S. P. Johnstone, A. J. Groszek, P. T. Starkey, C. J. Billinton, T. P. Simula, and K. Helmerson, Evolution of large-scale flow from turbulence in a two-dimensional superfluid, *Science* **364**, 1267 (2019).
- [25] M. T. Reeves, T. P. Billam, B. P. Anderson, and A. S. Bradley, Identifying a superfluid Reynolds number via dynamical similarity, *Phys. Rev. Lett.* **114**, 155302 (2015).
- [26] M. T. M. Christenhusz, A. Safavi-Naini, H. Rubinsztein-Dunlop, T. W. Neely, and M. T. Reeves, Emergent universal drag law in a model of superflow, *Phys. Rev. Lett.* **135**, 066001 (2025).
- [27] Y. Lim, Y. Lee, J. Goo, D. Bae, and Y. Shin, Vortex shedding frequency of a moving obstacle in a Bose–Einstein condensate, *New J. Phys.* **24**, 083020 (2022).
- [28] G. L. Eyink, Josephson–Anderson relation and the classical D’Alembert paradox, *Phys. Rev. X* **11**, 031054 (2021).
- [29] W. J. Kwon, S. W. Seo, and Y. Shin, Periodic shedding of vortex dipoles from a moving penetrable obstacle in a Bose–Einstein condensate, *Phys. Rev. A* **92**, 033613 (2015).
- [30] P. Engels and C. Atherton, Stationary and nonstationary Fluid Flow of a Bose–Einstein Condensate Through a Penetrable Barrier, *Phys. Rev. Lett.* **99**, 160405 (2007).
- [31] S. Finazzi, F. Piazza, M. Abad, A. Smerzi, and A. Recati, Instability of the superfluid flow as black-hole lasing effect, *Phys. Rev. Lett.* **114**, 245301 (2015).
- [32] X. Antoine and R. Duboscq, GPELab, a MATLAB toolbox to solve Gross–Pitaevskii equations I: Computation of stationary solutions, *Comput. Phys. Commun.* **185**, 2969 (2014).
- [33] X. Antoine and R. Duboscq, GPELab, a MATLAB toolbox to solve Gross–Pitaevskii equations II: Dynamics and stochastic simulations, *Comput. Phys. Commun.* **193**, 95 (2015).
- [34] T. Frisch, Y. Pomeau, and S. Rica, Transition to dissipation in a model of superflow, *Phys. Rev. Lett.* **69**, 1644 (1992).
- [35] T. P. Billam, M. T. Reeves, B. P. Anderson, and A. S. Bradley, Onsager–Kraichnan condensation in decaying two-dimensional quantum turbulence, *Phys. Rev. Lett.* **112**, 145301 (2014).
- [36] J. Huynh, F. Hébert, M. Albert, and P.-E. Larré, Critical velocity of a two-dimensional superflow past a potential barrier of arbitrary penetrability, *Phys. Rev. A* **109**, 013317 (2024).
- [37] J. Rønning and L. Angheluta, Precursory patterns to vortex nucleation in stirred Bose–Einstein condensates, *Phys. Rev. Research* **5**, 023108 (2023).
- [38] Z. Maches, E. Bartley, J. Borjon, and R. Carretero-González, Stability of finite and infinite von Kármán vortex-cluster streets, *Phys. Rev. E* **103**, 032205 (2021).
- [39] C. A. Jones and P. H. Roberts, Motions in a Bose condensate. IV. Axisymmetric solitary waves, *J. Phys. A: Math. Gen.* **15**, 2599 (1982).
- [40] S. Yoneda and H. Takeuchi, Proper orthogonal decomposition of a superfluid turbulent wake, *J. Phys. Soc. Jpn.* **94**, 073601 (2025).
- [41] M. T. Reeves, B. P. Anderson, and A. S. Bradley, Classical and quantum regimes of two-dimensional turbulence in trapped Bose–Einstein condensates, *Phys. Rev. A* **86**, 053621 (2012).
- [42] C. Huepe and M. E. Brachet, Scaling Laws for Vortical Nucleation Solutions in a Model of Superflow, *Physica D* **140**, 126 (2000).
- [43] C. Josserand, Y. Pomeau, and S. Rica, Vortex shedding in a model of superflow, *Physica D* **134**, 111 (1999).
- [44] S. Musser, D. Proment, M. Onorato, and W. T. M. Irvine, Starting flow past an airfoil and its acquired lift in a superfluid, *Phys. Rev. Lett.* **123**, 154502 (2019).
- [45] S. Rica, Vortex nucleation in a superfluid flow past an obstacle, in *Quantized Vortex Dynamics and Superfluid Turbulence*, Lecture Notes in Physics, Vol. 571, edited by C. F. Barenghi, R. J. Donnelly, and W. F. Vinen (Springer-Verlag, Berlin, Heidelberg, 2001), pp. 258–267.
- [46] T. Winiecki, B. Jackson, J. F. McCann, and C. S. Adams, Vortex shedding and drag in dilute Bose–Einstein condensates, *J. Phys. B: At. Mol. Opt. Phys.* **33**, 4069 (2000).
- [47] H. Kokubo, H. Takeuchi, K. Kasamatsu, Critical velocity for wake vortex generation behind a plate in a superfluid, *Phys. Rev. A* **111**, 043314 (2025).
- [48] C. Norberg, Fluctuating lift on a circular cylinder: review and new measurements, *J. Fluids Struct.* **17**, 57 (2003).
- [49] H. Takeuchi, Vortex Line Density in a Superfluid Turbulent Wake in the Zero Temperature Limit, *Ann. Phys.* **538**, 2500270 (2025).
- [50] For a sphere in a classical fluid at low Reynolds number, $C_D = 24 \text{ Re}^{-1}$ [1]. In contrast, for a circular cylinder, Oseen’s correction [51] leads to a different scaling exponent, $\alpha \equiv -\frac{d(\ln C_D)}{d(\ln \text{Re})} \simeq 1 - \frac{1}{2 - \ln \text{Re}} < 1$.
- [51] H. Lamb, On the uniform motion of a sphere through a

- viscous fluid, *Lond. Edinb. Dubl. Philos. Mag. J. Sci.* **21**, 112 (1911).
- [52] O. Cadot, Y. Couder, A. Daerr, S. Douady, and A. Tsinober, Energy injection in closed turbulent flows: Stirring through boundary layers versus inertial stirring, *Phys. Rev. E* **56**, 427 (1997).
- [53] K. P. Iyer, Turbulence without walls: whither the zeroth law of turbulence?, *Phys. Rev. Lett.* **135**, 134001 (2025).
- [54] I. Carusotto, Bogoliubov-Čerenkov radiation in a Bose-Einstein condensate flowing against an obstacle, *Phys. Rev. Lett.* **97**, 260403 (2006).
- [55] Z. Dutton, M. Budde, C. Slowe, and L. V. Hau, Observation of quantum shock waves created with ultra-compressed slow light pulses in a Bose-Einstein condensate, *Science* **293**, 663 (2001).
- [56] H. W. Liepmann and A. Roshko, *Elements of Gas dynamics* (Wiley, New York, 1957).
- [57] A. M. Kamchatnov and L. P. Pitaevskii, Stabilization of solitons generated by a supersonic flow of Bose-Einstein condensate past an obstacle, *Phys. Rev. Lett.* **100**, 160402 (2008).
- [58] P. A. Murthy and S. Jochim, Direct imaging of the order parameter of an atomic superfluid using matterwave optics, [arXiv:1911.10824 \[cond-mat.quant-gas\]](https://arxiv.org/abs/1911.10824).
- [59] S. Burger, K. Bongs, S. Dettmer, W. Ertmer, K. Sengstock, A. Sanpera, G. V. Shlyapnikov, and M. Lewenstein, Dark solitons in Bose-Einstein condensates, *Phys. Rev. Lett.* **83**, 5198 (1999).
- [60] G. Del Pace, K. Xhani, A. Muzi Falconi, M. Fedrizzi, N. Grani, D. Hernandez Rajkov, M. Inguscio, F. Scazza, W. J. Kwon, and G. Roati, Imprinting persistent currents in tunable fermionic rings, *Phys. Rev. X* **12**, 041037 (2022).
- [61] J. Denschlag, J. E. Simsarian, D. L. Feder, C. W. Clark, L. A. Collins, J. Cubizolles, L. Deng, E. W. Hagley, K. Helmerson, W. P. Reinhardt, S. L. Rolston, B. I. Schneider, and W. D. Phillips, Generating solitons by phase engineering of a Bose-Einstein condensate, *Science* **287**, 97 (2000).
- [62] C.-T. Pham, C. Nore, and M.-E. Brachet, Boundary layers in Gross-Pitaevskii superflow around a disk, *C. R. Phys.* **5**, 3 (2004).
- [63] Far downstream of the obstacle, the vorticity width was found to scale as \sqrt{s} , where s is the distance from the obstacle, consistent with the 2D classical wake-width scaling [11].